Reduction of oxygen content in laser powder bed fusion process atmosphere – Effects on stochastic defect formation and mechanical properties

Citation for the original published paper (version of record):

de Andrade Schwerz, C., Moverare, J., Küng, A. et al (2024). Reduction of oxygen content in laser powder bed fusion process atmosphere – Effects on stochastic defect formation and mechanical properties. Journal of Materials Research and Technology, 30: 4667-4681. http://dx.doi.org/10.1016/j.jmrt.2024.04.177

Journal of Materials Research and Technology 30 (2024) 4667–4681

Contents lists available at ScienceDirect

Journal of Materials Research and Technology

journal homepage: www.elsevier.com/locate/jmrt

Reduction of oxygen content in laser powder bed fusion process atmosphere – Effects on stochastic defect formation and mechanical properties

Claudia Schwerz [a,*], Johan Moverare [b], Alain Kung [c], Benjamin A. Bircher [c], Dmitri Riabov [a,d], Lars Nyborg [a]

[a] Chalmers University of Technology, Department of Industrial and Material Science, Sweden
[b] Linköping University, Department of Management and Engineering, Sweden
[c] Federal Institute of Metrology METAS, Laboratory for Length, Nano- and Microtechnology, Switzerland
[d] Höganäs AB, Sweden

ARTICLE INFO

Handling Editor: L Murr

Keywords:
In-situ monitoring
Defect detection
Defect mitigation
Oxidation
Spatter
Fatigue

ABSTRACT

Stochastic defects in materials manufactured via laser powder bed fusion (LPBF) can severely compromise mechanical performance and are challenging to predict and detect, thus motivating the development of defect mitigation strategies. Particle oxidation is a factor well-known to generate defects by disturbing melt pool dynamics. If the particles are spatters, additional disturbances increase the likelihood of defect formation. In this study, restricting oxygen content in the process atmosphere to 50 ppm is investigated to minimize stochastic spatter-induced defects and improve the mechanical properties of Hastelloy X. Specimens were manufactured under this condition at two nominal layer thicknesses, analyzed for internal defects, and mechanically tested. Contrary to expectations, reducing the oxygen content did not prevent spatter-induced defect formation; rather, it could exacerbate the formation of more numerous and larger defects. Nevertheless, this tighter control of the process atmosphere led to significant microstructural refinement, which, when combined with sparse defects, resulted in improved fatigue performance. Despite the inherent ductility of Hastelloy X, the presence of abundant defects significantly larger than the microstructural characteristic size proved detrimental to fatigue performance. Notably, the occurrence of defects exhibited considerable variation across the build area, contributing to scatter in fatigue data. However, quantitative analysis of in-situ monitoring data enabled prediction of variability in defect content and mechanical performance.

1. Introduction

Defect formation occurring despite process optimization jeopardizes the performance of materials manufactured via laser powder bed fusion (LPBF) and the process' reliability. Particularly, the inconsistent fatigue performance of LPBF materials is a widely reported issue [1] that has been attributed mainly to surface characteristics [2] and internal defects [3], especially large, irregularly shaped lack of fusion [4]. Although all internal defects potentially compromise the mechanical performance of materials, those formed stochastically present greater challenges in terms of criticality, predictability, and detection. Furthermore, one of their formation mechanisms is dependent on an unavoidable phenomenon in LPBF, namely the formation of process byproducts [5,6]. Therefore, it is essential to develop strategies that can effectively reduce their occurrence in-process.

One of the intrinsic process byproducts that can promote formation of stochastic defects in LPBF are spatters [5,7,8]. These particles are generated in-process, ejected upon the interaction of the laser beam with the powder bed, interact with the process atmosphere and oxidize [9], and are carried by the process gas out of the build area. Typically, not all particles are effectively removed, and can redeposit on the powder bed, thus contributing to powder degradation [10,11] and to defect formation, in case the deposition occurs on the surface of a part ongoing manufacturing [6,12].The exact contribution of spatter characteristics on defect formation is still unclear, but the presence of the particle itself, its size and surface characteristics have been reported as contributing factors. The presence of the particles on the powder bed per se, particularly those of large dimensions, prompts a local increase in the thickness of the powder layer [13] and attenuates the laser beam [14], thus hampering complete fusion and consequently forming defects. Their

---

* Corresponding author.
E-mail addresses: claudia.schwerz@chalmers.se, cschwerz@outlook.com (C. Schwerz).

https://doi.org/10.1016/j.jmrt.2024.04.177
Received 26 February 2024; Received in revised form 19 April 2024; Accepted 19 April 2024

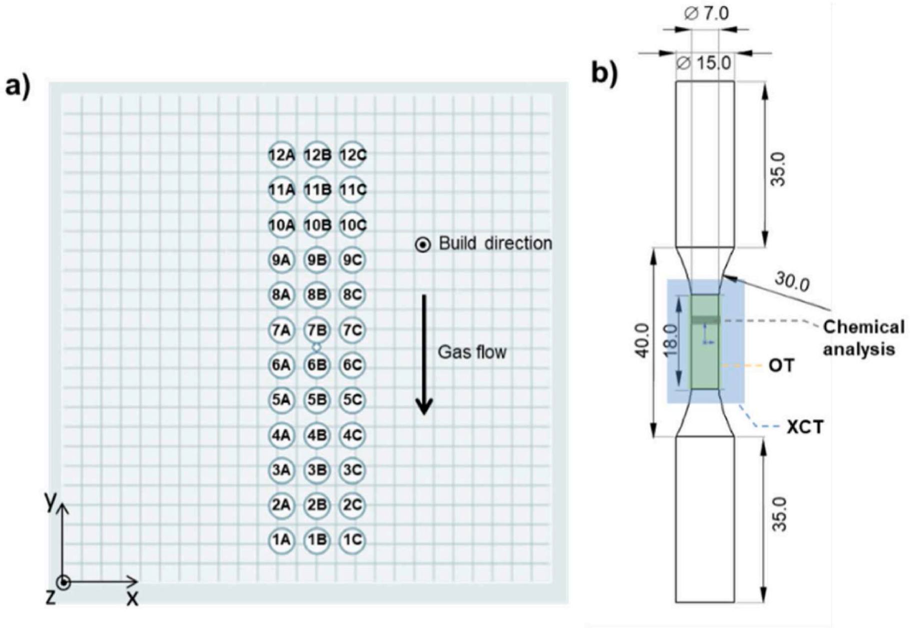

Fig. 1. a) Top view of the build layout with specimen identification. b) Geometry and nominal dimensions of the as-printed specimens. The regions where different analyses were made are indicated: XCT (in blue), OT (in green), and the bulk chemistry (in grey).

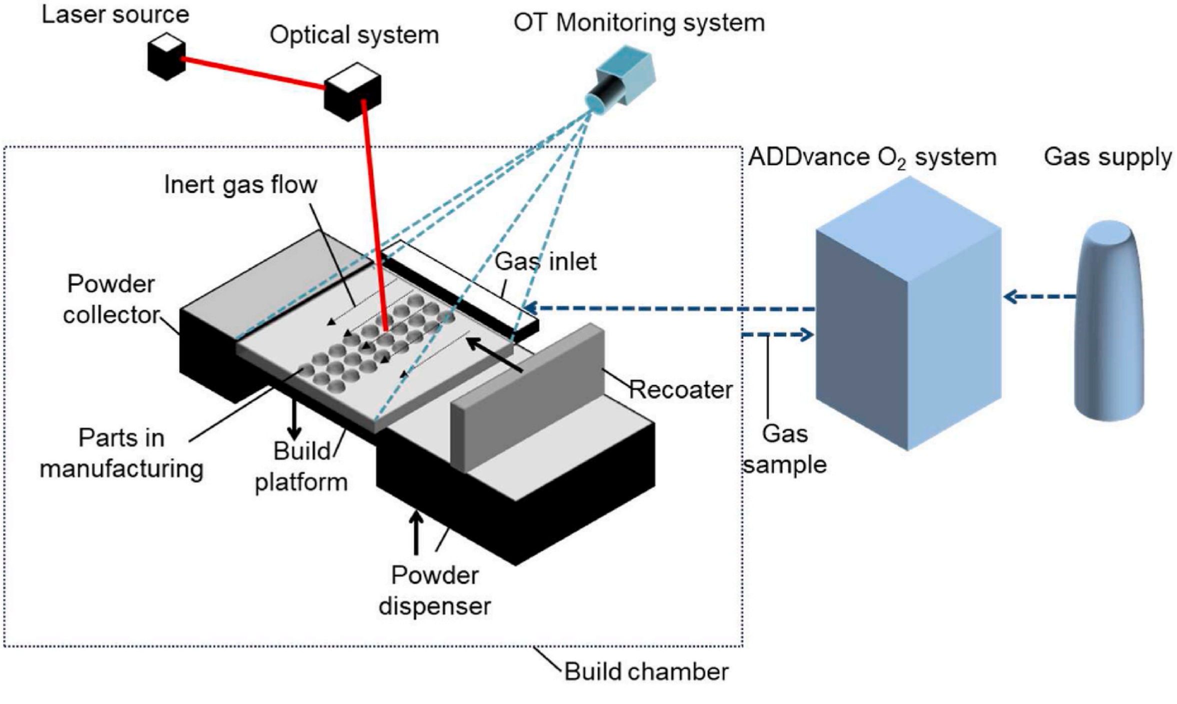

Fig. 2. Schematic of the manufacturing process, monitoring and oxygen control setup.

surface oxidation has also been attributed to induce contamination and defect formation [15,16] by altering the melt pool dynamics, and possibly promoting defect nucleation, stabilization and growth [17]. The oxidized surface has also been reported to increase the absorption of laser irradiation, thus increasing recoil pressure and surface tension variations, which boosts spattering and defect formation upon their redeposition [18].

The process atmosphere plays a major role on the surface characteristics of spatter and resulting bulk chemical composition [19]. Using varying levels of oxygen in the process atmosphere, Raza et al. [20] observed that the quantity and thickness of oxide patches and particulates was directly proportional to the oxygen content in the build chamber. In a previous study [21], it was found that restriction of the oxygen content in the process atmosphere to a maximum of 50 ppm left Hastelloy X particles covered with an oxide thickness similar to that of the virgin powder, instead of a 10-fold increase experienced in a most commonly used process atmosphere containing 1000 ppm oxygen. This suggests that a process atmosphere containing maximum 50 ppm oxygen might reduce or even prevent spatter-induced defect formation, by preventing the formation of a thick surface oxide layer. Moreover, as the restriction of oxygen content to 50 ppm led to a smaller difference in the surface oxide layer thickness of spatters collected in different locations

Table 1
Processing conditions in the different sets of specimens, including reference sets 1 and 2.

Build ID	Maximum oxygen content in the process atmosphere	Nominal layer thickness
Set A	50 ppm	80 μm
Set B	50 ppm	120 μm
Set 1 [26]	1000 ppm	80 μm
Set 2 [26]	1000 ppm	120 μm

of the build chamber [21], there is a potential for higher homogeneity in the defect populations in parts manufactured across the build area.

In terms of the effect varying oxygen contents might have on the mechanical properties of LPBF material, the reduction of oxygen content has been reported to decrease the ultimate tensile strength of Ti–6Al–4V [22], presumably due to the interstitial solid solution strengthening effect of this element in a titanium matrix. Such effect is not present for other alloy systems, e.g. Hastelloy X and stainless steels, due to the anion radius being too large to accommodate interstitially [23]. In this case, oxygen can form oxides or inclusions [23] depending on the alloy system and thermal history.

In this study, Hastelloy X, a nickel-based superalloy solid-solution strengthened by the high amounts of alloying elements chromium, iron, and molybdenum, is the analyzed material. Differently from other Ni-based superalloys, it is not enriched with precipitation-forming elements. On the other hand, this alloy is susceptible to carbide formation at grain boundaries, in particular after high-temperature service or heat treatment [24] This nickel-based superalloy presents a favorable printability in comparison to other superalloys [25] i.e., the alloy has low susceptibility to metallurgical cracking. Thus, the defect formation mechanisms studied in this paper can be readily isolated and controlled.

In this study, the effect of reduction of oxygen content in the process atmosphere on spatter-induced stochastic defect formation and mechanical properties of Hastelloy X are studied. For that, the manufacturing and testing experiments documented in previous work [26] are taken as baseline and reproduced with the oxygen content in the process atmosphere restricted to a maximum of 50 ppm. Since stochastic defect formation related to spattering is more significant when the powder layer thickness is larger [6,27], nominal layer thicknesses of 80 μm and 120 μm are used. The build jobs are monitored with optical tomography for detection of defect-inducing spatter redeposits. Selected specimens are measured via X-ray computed tomography (XCT). The specimens are fatigue tested at two stress ranges and their fracture surfaces are analyzed and correlated with their fatigue performance. This study reveals the potentials and limitations of tighter process atmosphere control in LPBF, in terms of defect mitigation and mechanical property enhancement. Furthermore, this study underscores the importance of in-situ monitoring for predicting defect variability and mechanical performance.

2. Materials and methods

2.1. Laser powder bed fusion manufacturing

Test specimens were manufactured using gas atomized Hastelloy X powder from Höganäs AB in a M290 (EOS GmbH) laser powder bed fusion machine, as per the layout in Fig. 1, with 36 specimens laid on a 3 × 12 grid. EOS M290 was connected to an ADDvance® O_2 precision system (Linde GmbH) to achieve a process atmosphere with maximum 50 ppm oxygen. The system works by purging additional inert gas (argon) into the build chamber until the desired condition is obtained. During the entire build process, argon gas flow is sustained, the oxygen concentration is measured via a chemical cell, and controlled by adjusting the inert gas flow, as schematized in Fig. 2.

Two build jobs (sets A and B) were performed for this study, using identical processing conditions, except for the nominal layer thickness,

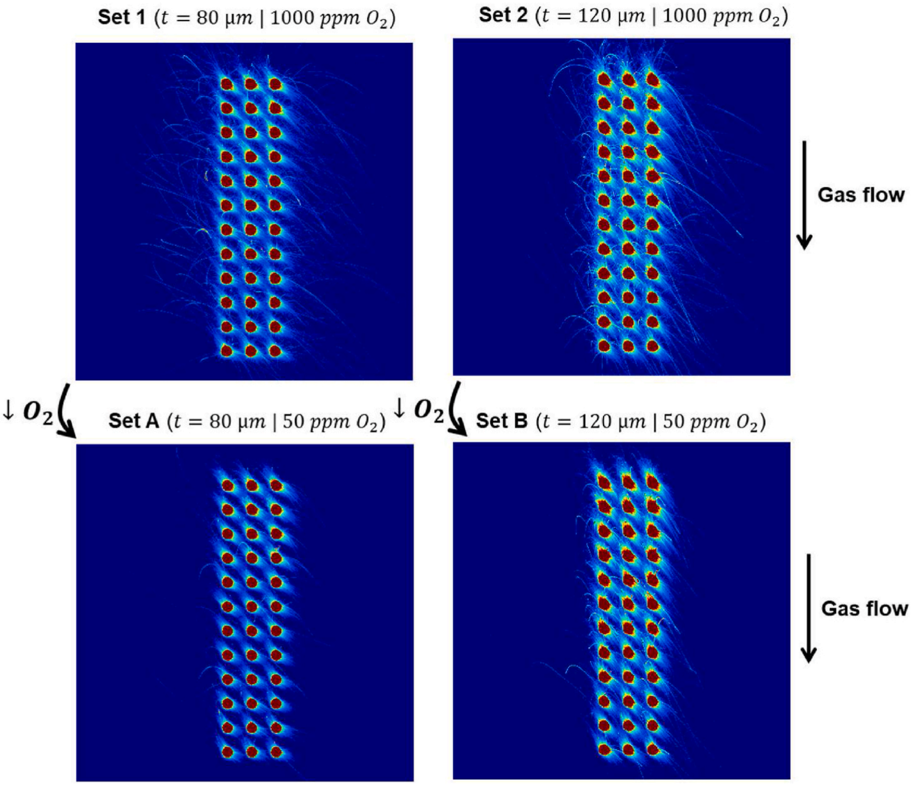
Set 1 ($t = 80\ \mu m$ | $1000\ ppm\ O_2$)
Set 2 ($t = 120\ \mu m$ | $1000\ ppm\ O_2$)
Set A ($t = 80\ \mu m$ | $50\ ppm\ O_2$)
Set B ($t = 120\ \mu m$ | $50\ ppm\ O_2$)

Fig. 3. Representative pseudocolor OT images with enhanced brightness revealing spatter trajectories in geometrically identical build jobs. The nominal layer thicknesses t and the oxygen contents in the process atmosphere are indicated. The gas flow direction and settings are identical in all images.

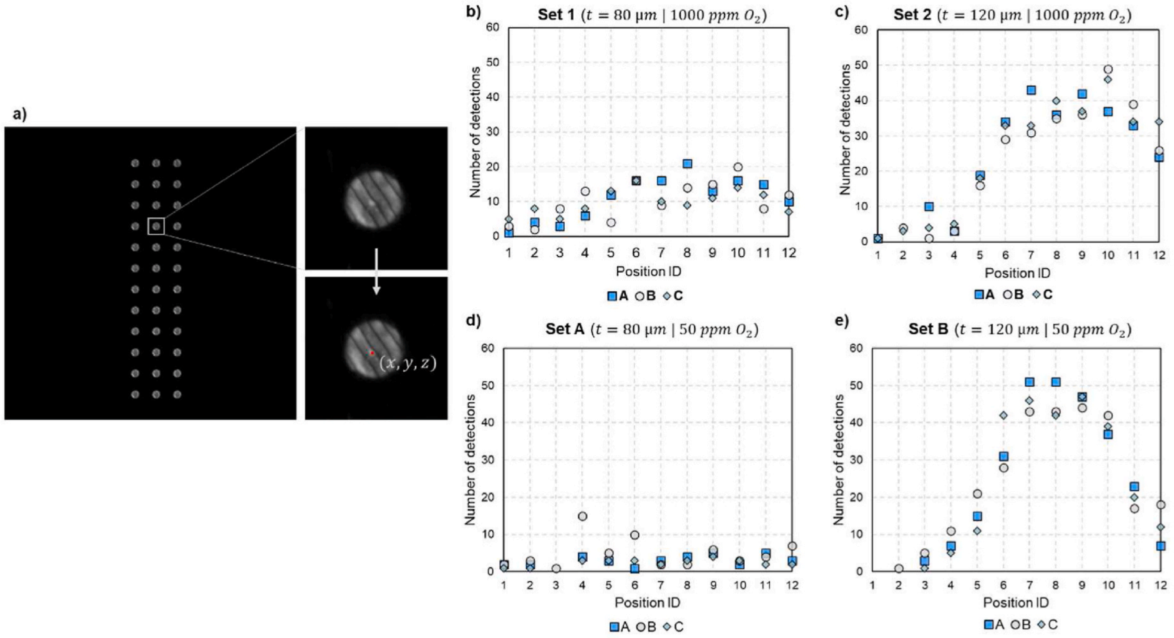

Fig. 4. Quantitative analysis of OT images. (a) Scheme of the spatter redeposition detection procedure. (b–e) Number spatter detections in OT images during manufacturing of the gauge sections of specimens in sets A, B and reference sets 1 and 2 [26].

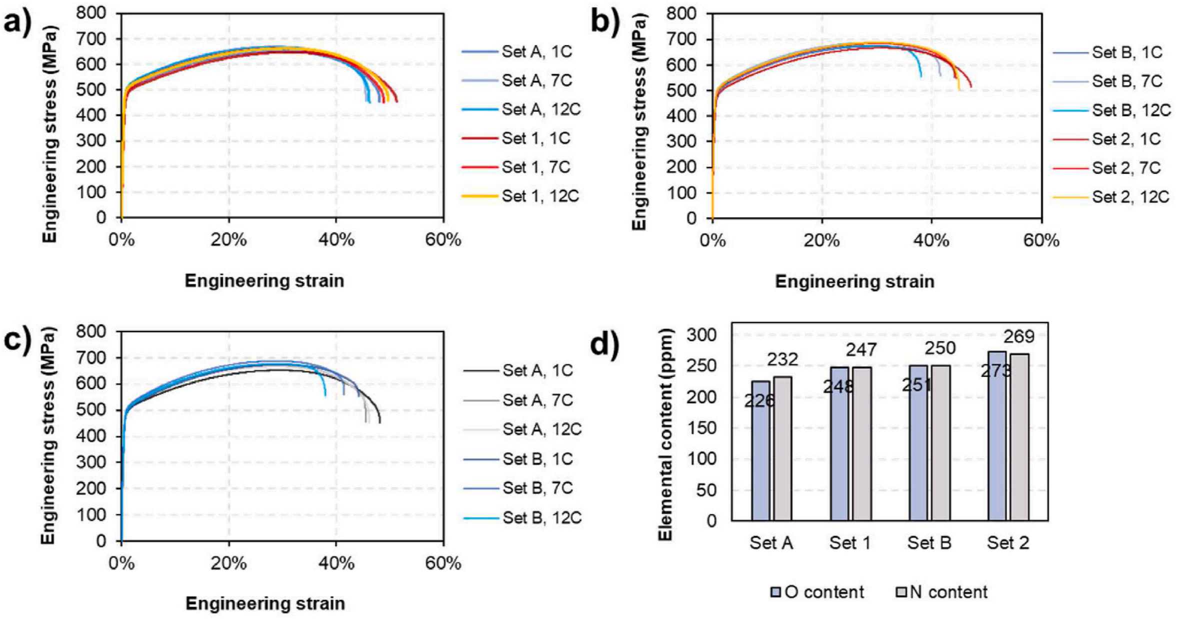

Fig. 5. Comparative tensile properties of specimens in sets A and 1 (a), sets B and 2 (b), and sets A and B (c). (d) Bulk oxygen and nitrogen contents.

which simultaneously drives the process productivity [28] and spatter-induced defects [6]. Sets A and B, manufactured in a process atmosphere containing a maximum of 50 ppm oxygen, are compared to sets 1 and 2, investigated in previous work [26]. Sets 1 and 2 were manufactured in a process atmosphere with maximum 1000 ppm oxygen, and are otherwise identical to sets A and B, respectively, as specified in Table 1.

All sets of specimens were manufactured with a rotating scan pattern (67° rotation between consecutive layers), 80 °C build platform preheating, and an EOS grid nozzle to allow the flow of argon gas into the build chamber.

The processing parameters used were selected to produce virtually defect-free bulk material, with defect contents less than 0.05% [12]. The parameters are laser power of 370 W, laser scan speed of 1000 mm/s and hatch spacing of 100 μm, identically to previous work [12,26].

2.2. Monitoring of laser powder bed fusion and detection of spatter redeposits

The M290 machine is equipped with the EOSTATE monitoring suite (EOS GmbH), which includes optical tomography (OT) as a monitoring system. The OT system contains a sCMOS (scientific complementary metal-oxide-semiconductor) camera, installed outside the build chamber, that provides a top view of the whole build area (Fig. 2). The camera is equipped with a bandpass filter to avoid detection of environmental noise. Images are acquired continuously during the exposure of a print

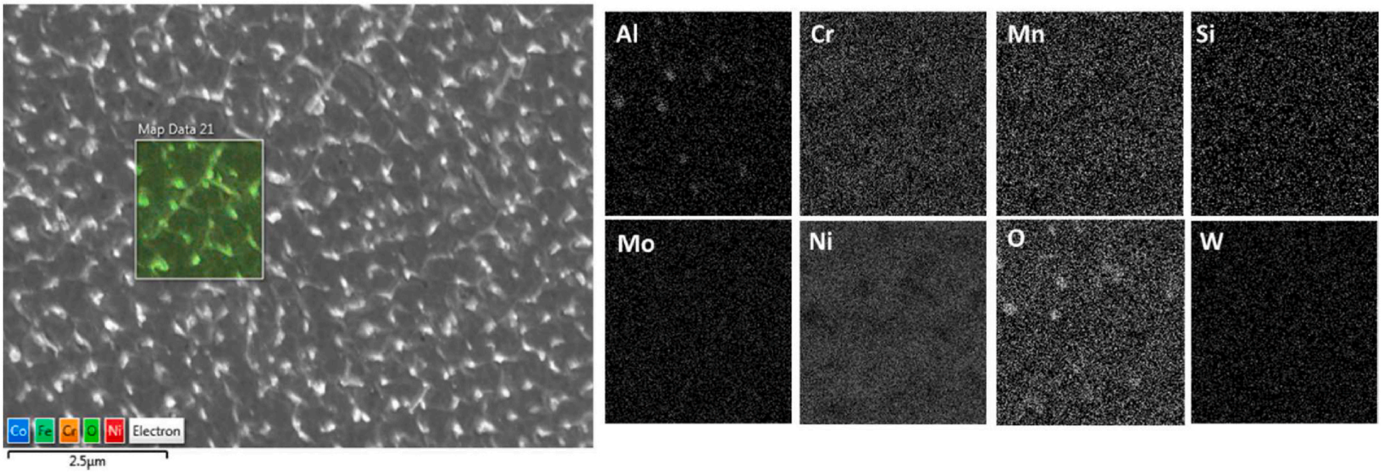

Fig. 6. EDS map of the cellular structure present in LPBF Hastelloy X. A sample in set 1 is represented in the image.

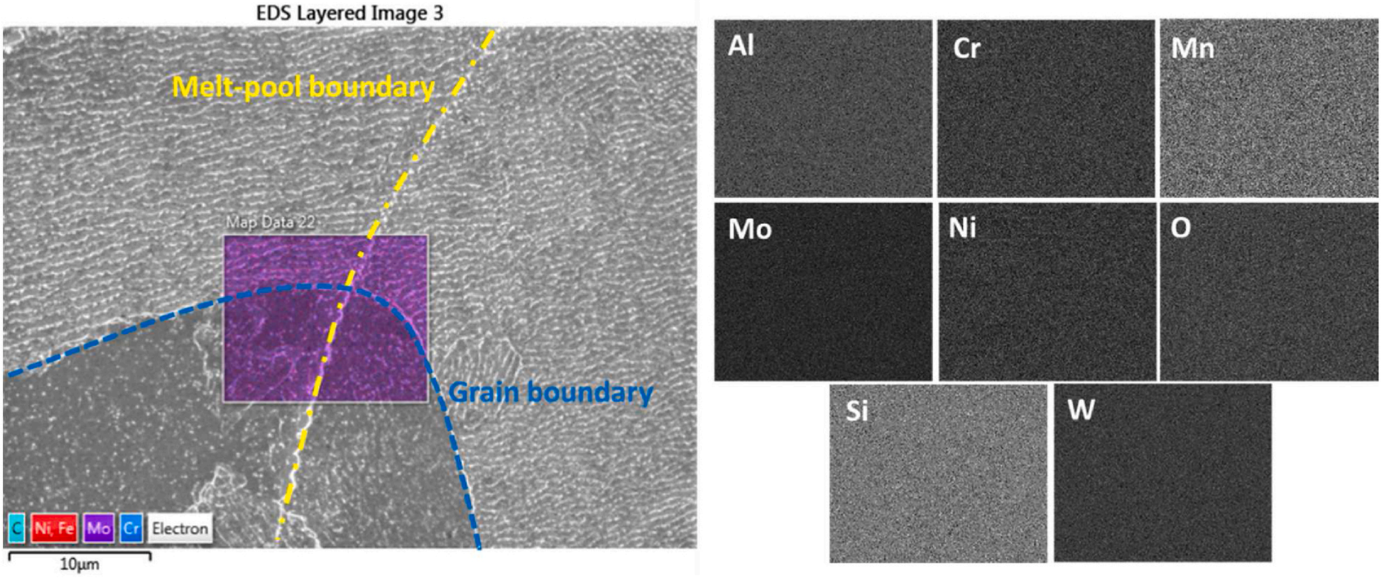

Fig. 7. EDS map of a region containing a melt pool boundary and a grain boundary. A sample in set 1 is represented.

layer with exposure time of 0.1s. These images are then combined within the system, generating two outputs: a *MAX* image, in which each pixel represents the maximum intensity on regions of size 125 μm × 125 μm, and an *INT* image, where each pixel represents the integral intensities in these regions. Geometrical and intensity corrections are applied. Thus, EOSTATE OT outputs one *MAX* and one *INT* image of dimensions 2000 × 2000 pixels per print layer of the entire build job. EOSTATE OT was used for data acquisition only; data processing and analysis were performed in a Matlab environment.

Spatter redeposits manifest as bright blobs on MAX OT images [6, 12]. Thus, to detect spatter redeposits, MAX OT images were analyzed for blob detection through convolution with a Laplacian of Gaussian filter and subsequent non-minimum suppression, following the methodology developed in earlier research [6].

2.3. Mechanical testing

Machined, grinded and polished specimens were fatigue tested at room temperature, following the procedures recommended in ISO 1099. With the post-processing of the specimens, the resulting gauge diameters were 6.0 mm. The fatigue tests were stress-controlled, with two test stress ranges, 800 MPa and 900 MPa, and stress ratio $R = -1$. Cyclic loading with frequency of 10 Hz was used.

Additionally, tensile tests were conducted in as-printed specimens, with geometry and dimensions illustrated in Fig. 1b. The tensile tests were conducted at room temperature on a Instron 5582 universal electromechanical testing machine with a 100 kN load cell, at a constant strain rate of 2·10-3 s^{-1}, according to the procedures recommended in the ISO 6892-1 standard.

2.4. Fractographic analysis

After mechanical testing, fractographic analysis was performed. Firstly, a Zeiss Discovery V20 stereo optical microscope (SOM) was used, then a LEO Gemini 1550 scanning electron microscope (SEM).

2.5. X-ray computed tomography

Prior to fatigue testing, the gauge sections of selected machined specimens were inspected via X-ray computed tomography (XCT) to measure internal defects. The XCT system consists of a microfocus X-ray tube, operated at a voltage of 180 kV and 15 W target power, a flat panel

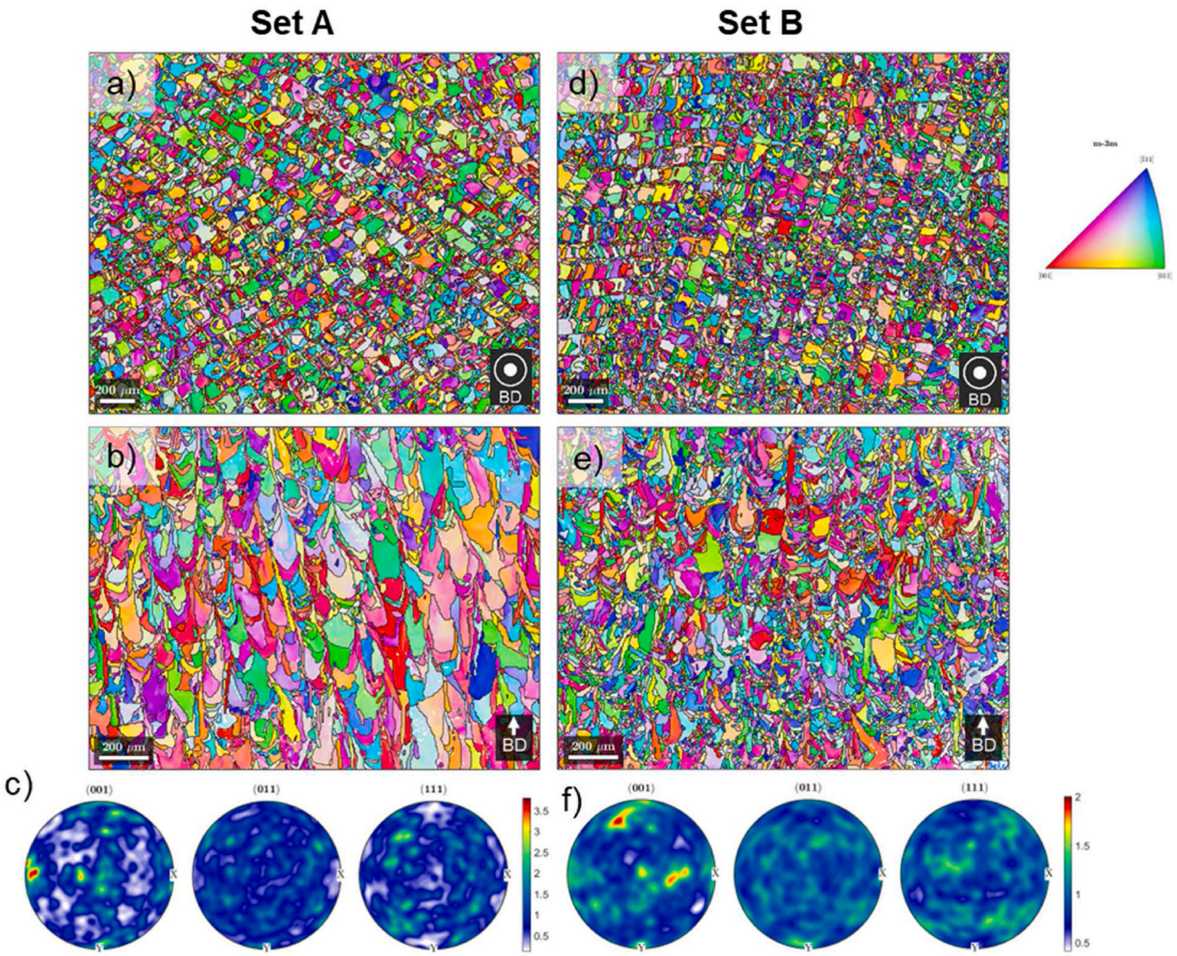

Fig. 8. EBSD orientation maps perpendicular to (a, b) and along the build direction (BD) (c, d) in sets A and B. Also shown are the (001), (011), and (111) pole figures from both sets, the pole figures originate from the maps in b and e.

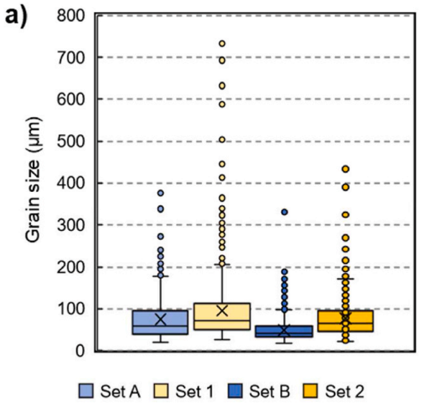

b)

Build ID	Nominal layer thickness (μm)	Maximum oxygen content in the process atmosphere (ppm)	Average grain size (μm)
Set A	80	50	74
Set 1	80	1000	95
Set B	120	50	49
Set 2	120	1000	77

Fig. 9. a) Grain size distributions (fitted ellipse major diameter) measured on EBSD maps oriented parallel with the building direction. The crosses represent the average values, also presented on the table (b).

X-ray detector, and air-bearing motion axes. The acquired data were analyzed in VG Studio MAX 3.4 (Volume Graphics). XCT volume data with a resolution of 4.36 μm were analyzed for defect characteristics, such as defect size, sphericity, and positions, the latter given by the centers of the spheres circumscribing the defects. Further details on the XCT system and data analysis method are described in previous work [26].

2.6. Material characterization

Material characterization techniques were used to a limited extent, to help explain the measured mechanical performance of Hastelloy X beyond the presence of defects.

Chemical analysis was performed to determine bulk oxygen and nitrogen contents using a LECO ON836. In this equipment, samples were placed into a graphite crucible and heated to release analyte gases,

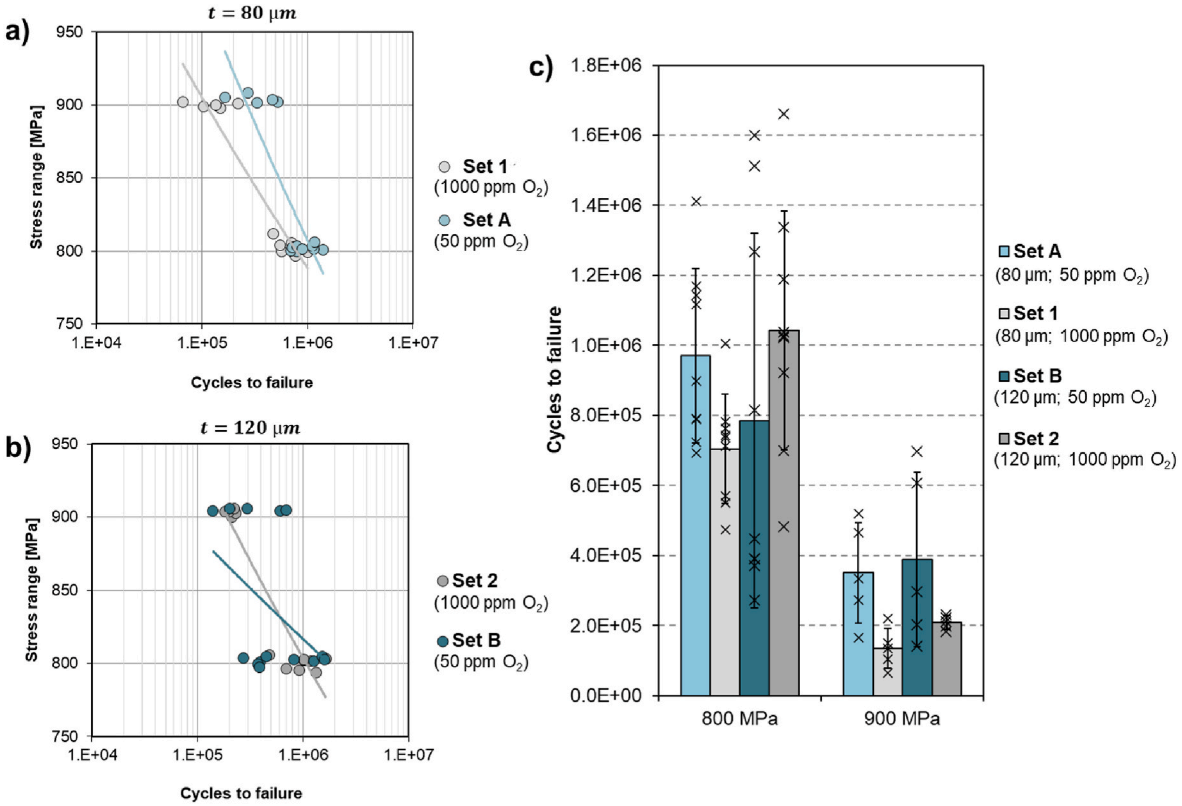

Fig. 10. Summary of fatigue properties of HX manufactured in process atmospheres with varying oxygen contents. S–N curves for HX manufactured with maximum oxygen content of 50 ppm vs. 1000 ppm and nominal layer thickness 80 μm (a) and 120 μm (b). Alternative visualization of the data is provided in (c), showing the average life of each set of specimens for the target stress ranges 800 MPa and 900 MPa. Individual data points are marked with a cross. The error bars represent one standard deviation from the average.

which were detected by non-dispersive infrared (NDIR) cells.

For electron backscattered diffraction (EBSD) analysis, the gauge section of specimen 7A (as per Fig. 1) was sectioned on planes parallel and perpendicular to the build direction. Specimen preparation was conducted with the following steps: mounting in conductive resin, plane grinding using 500 grit SiC paper, fine grinding using a 9 μm diamond suspension, polishing using 3 and 1 μm diamond suspensions, and final polishing using a suspension of colloidal silica for 20 min. The EBSD maps were acquired in a Leo Gemini 1550 SEM equipped with a Nordlys II detector by Oxford Instruments, with an accelerating voltage of 20 kV and a step size between 7 and 3.5 μm. Data analysis was done with the MTEX toolbox [29]. Energy-dispersive x-ray spectroscopy (EDS) was acquired using low accelerating voltage of 5 kV to reduce the interaction volume using an Oxford Instruments X-Max detector.

3. Results

3.1. Spatter formation and redeposition observed via optical tomography monitoring

Fig. 3 shows pseudocolor OT images representative of each build in the gauge section. The brightness was enhanced identically in the images, and the layers represented are located at similar build heights. This representation of OT data has been previously used in the literature to provide a qualitative assessment of the extent of spatter formation [30, 31]. Based on that, the images reveal that with restriction in the oxygen content, smaller extensions of the build area are affected by signals in mid-range intensities, indicating a reduction in spatter formation for both nominal layer thicknesses used. The larger the nominal layer thickness, the more substantial is the spatter formation in a single layer [31] in both conditions of the process atmosphere (maximum 1000 ppm and 50 ppm oxygen). Thus, Fig. 3 visually indicates that reduction of oxygen content in the process atmosphere has a potential in reducing spattering.

Quantitative analysis of OT images, in the form of detection of spatter redeposits on the powder bed, was performed and is schematized in Fig. 4a. The number of detections within the gauge section of each specimen can be seen in Fig. 4b–e. There is a reduction in spatter redeposition associated to oxygen content restriction for nominal layer thickness of 80 μm (from set 1 to set A), in accordance with the qualitative indications in Fig. 3. The same modification in the process atmosphere when using a nominal layer thickness of 120 μm, however, did not necessarily reduce the number of potentially defect-forming spatter redeposits, despite the qualitative indication in Fig. 3. In fact, a higher number of spatter redeposits were detected within the gauge sections of the specimens manufactured in the mid to upper half of the build plate (positions 6–10 as per Fig. 1b) for set B than for set 2. Thus, the qualitative analysis of OT images highlighting spatter trajectories, and potentially the extension of spatter formation, do not necessarily correspond to the extent of spatters that redeposit within part boundaries and have the potential to form defects. The defect populations of both sets of material are measured by XCT, thus providing ground truth data, in section 3.3.1.

3.2. Tensile properties and microstructure

Although this study is centered on the evaluation of the influence of spatter on the fatigue life of LPBF Hastelloy X manufactured in a process atmosphere with low oxygen content, an assessment of the tensile properties of this material was also conducted. Three specimens from each set, namely those manufactured in positions 1C, 7C and 12C, as per Fig. 1B, were tensile tested in the as-printed condition. The measured

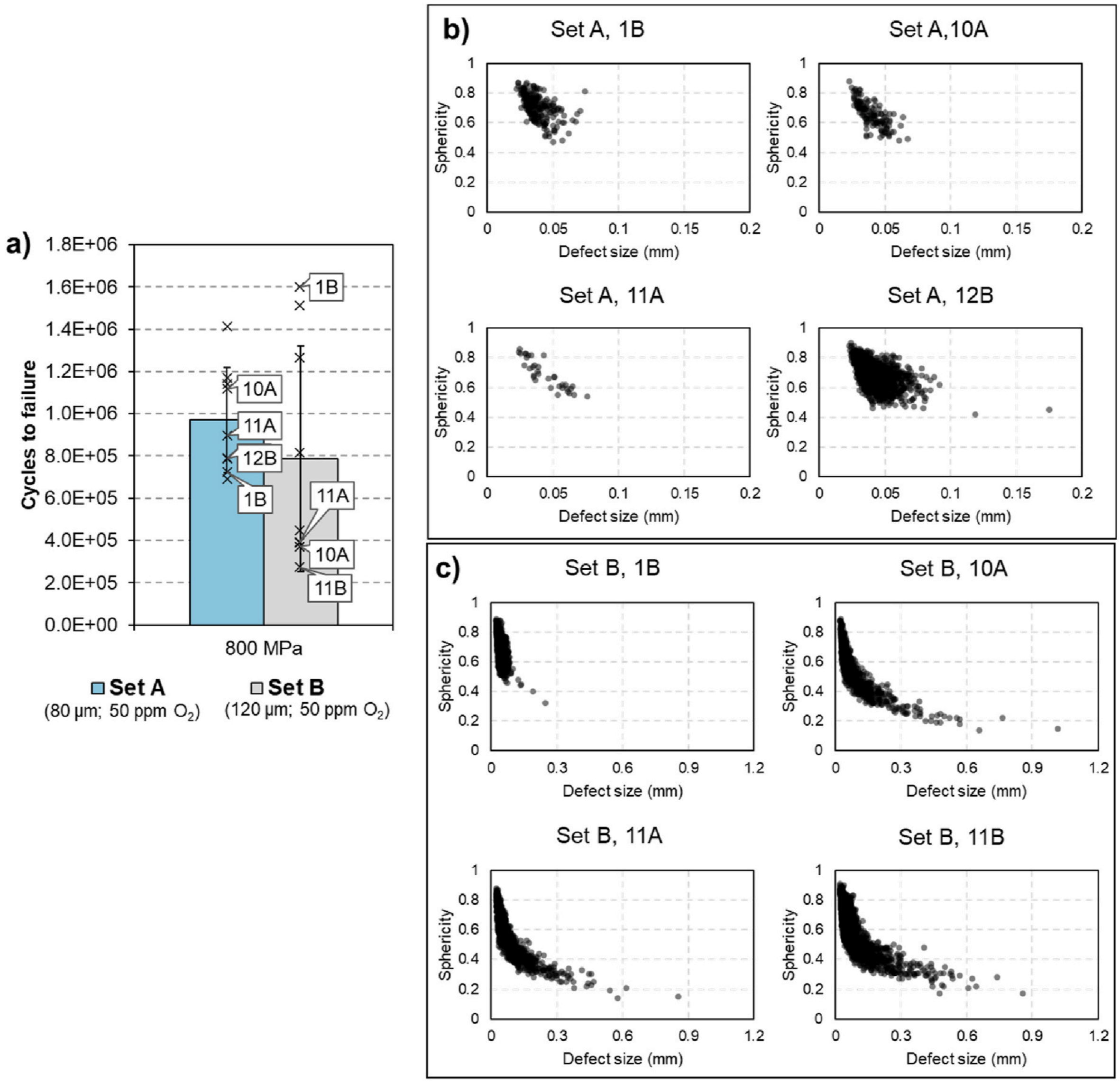

Fig. 11. Internal defects identified via XCT in eight fatigue specimens. a) Fatigue performance of the measured specimens highlighted in their groups. The target stress range (800 MPa) is indicated. Defect size vs. defect sphericity for four specimens in sets A (b), and B (c).

properties are summarized in Fig. 5, and listed in Table 2 in the Appendix. Comparing sets A and B with sets 1 and 2, respectively, the decrease in atmospheric oxygen content did not provoke any substantial differences in the tensile and yield strength, but a slight reduction in the elongation at fracture (Fig. 5 a, b). In both cases, the reduction of the atmospheric oxygen content from 1000 ppm to 50 ppm yielded a reduction of around 22 ppm oxygen and 17 ppm nitrogen in the bulk composition (Fig. 5 d). This compositional difference is due to the lower partial pressure of atmospheric gases in the build chamber resulting from the higher partial pressure of argon instead [22].

Regarding the influence of nominal layer thickness in a setup with enhanced control of the process atmosphere (set A vs. set B, Fig. 5 c), the average yield and tensile strengths are not significantly different between the two sets of data, while a decrease in elongation at fracture is observed for specimens built with higher productivity (set B). Similarly to prior work [26], an increase in nominal layer thickness is followed by a relative increase in the bulk oxygen content (in this case of 26 ppm between sets A and B).

Further investigation on the elementary distribution in the microstructure was conducted, with particular focus on the distribution of oxygen. Fig. 6 shows the typical cell structure found in Hastelloy X manufactured by LPBF, which consists of high-density dislocation walls [32,33]. Oxygen segregated to the cell boundaries as oxides [34] (seen as white dots), which were found to be primarily rich in Al. Such elemental segregation may be a contributing factor on the formation of the cellular structures [35,36]. When examining other potential elemental segregation sites, i.e., melt pool and grain boundaries, no measurable segregation could be identified (Fig. 7).

Electron backscattered diffraction (EBSD) orientation maps originating from sets A and B on planes parallel and perpendicular to the build direction are presented below in Fig. 8, while the measured grain size distributions are presented in Fig. 9. The grain morphology in both sets had typical for LPBF appearance with elongated grains and melt-pool-like shapes. In the maps oriented perpendicularly to the building direction, traces of the laser hatch spacing could be discerned. Set B presented significantly finer microstructure than set A, as its larger nominal layer thickness combined with the same melt pool dimensions of set A entails a smaller remelted volume in each layer, consequently a weaker tendency to grain growth [28]. The texture was also analyzed in the two sets, where no strong preferential texture was found in any of the investigated poles. Although, the maximum intensity Set B was even lower compared to Set A, indicating that the lower remelted volume

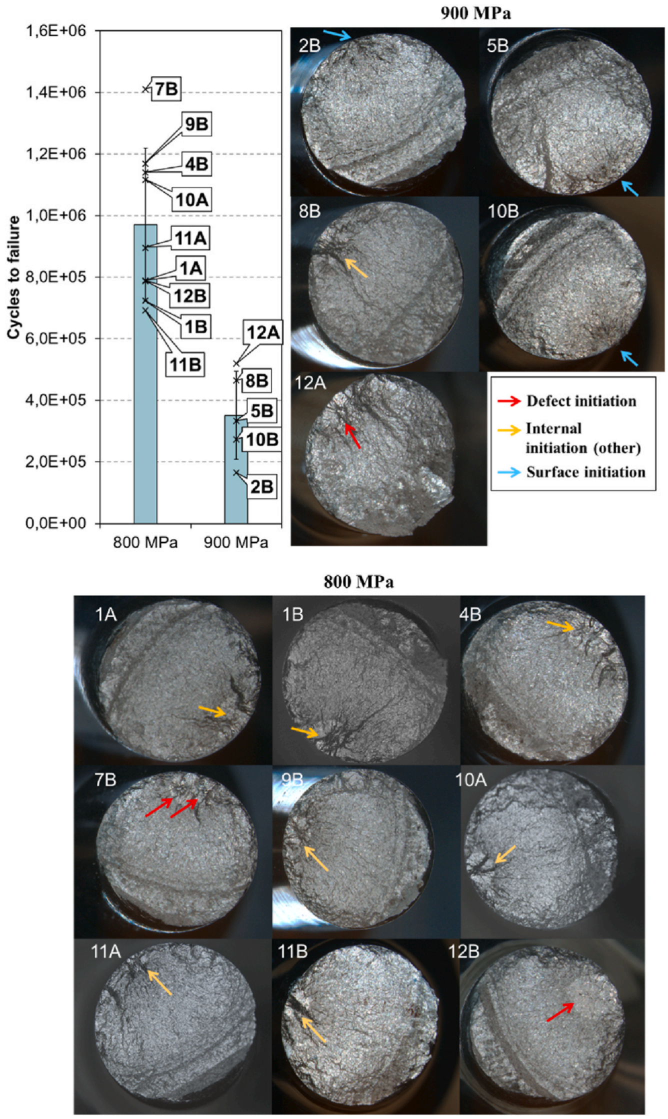

Fig. 12. Fracture surfaces of fatigue specimens in set A. The target stress ranges are indicated. The crack initiation sites are color-coded according to the type of initiation. The performance of each specimen is shown for reference.

inhibits the development of a strong texture within the material. Additionally, it was noticeable that both sets A and B produced with lower oxygen content presented finer microstructure than their baselines, presumably due to the increased gas flow in the building chamber, needed to sustain the tight control of the process atmosphere.

3.3. *Fatigue properties*

The fully-reversed stress-controlled fatigue test results are presented in this section, both for sets A and B and for the reference sets 1 and 2 [26] when applicable. The individual test results for sets A and B can be found in Table 3 in the Appendix. For specimens manufactured with a nominal layer thickness of 80 μm, a considerably higher average life was measured if tighter control of the process atmosphere had been applied (set A vs. set 1), as observed in Fig. 10 a and c. Namely, increases of 38% and 160% were measured for the 800 MPa and 900 MPa stress ranges, respectively. For specimens manufactured with a higher productivity, i.e., nominal layer thickness of 120 μm, the tighter control of the process atmosphere promoted a 85% increase in life for the higher test stress condition (set B vs. set 2, Fig. 10c). For the lower test stress condition, a 25% reduction in the average life was observed instead. A significantly larger scatter in life was observed in set B in both stress ranges.

Considering the difference in fatigue performance promoted by the nominal layer thickness employed, set A outperforms set B at the lowest test stress range, while a comparable performance was observed at the highest test stress range. This result is surprising, considering the much finer microstructure observed in set B (Fig. 8), and the corresponding comparison between sets 1 and 2, in which the finer microstructure of set 2 promoted higher average life despite its more substantial defect population [26]. The reasons for this behavior are investigated in the next subsections.

3.3.1. *Defects measured via X-ray computed tomography*

The gauge sections of four specimens of each of the sets A and B were measured via XCT post-machining and pre-testing. Fig. 11 shows the internal defect populations of these specimens, highlighting defect size and sphericity, which distinguish pores from lack of fusion (LoF) [12, 37]. The fatigue performance of these specimens is also presented for reference. In set A, the specimens contained mostly defects with the characteristics of pores in the gauge section. The only exception is specimen 12B, which presented two defects matching lack of fusion characteristics with sizes 175 μm and 119 μm. These results match the quantitative analysis of OT data (Fig. 4d), that revealed low quantity of spatter redeposition in the specimens of set A. Nonetheless, the restriction in the oxygen content to 50 ppm did not completely prevent the formation of lack of fusion. Similarly to observed in regular process atmosphere (1000 ppm O_2) [26], these sparse lack of fusion defects do not necessarily impact the fatigue performance of Hastelloy X.

In set B, all four specimens contained defects with lack of fusion characteristics in the gauge section. Three of these specimens contained a large quantity of said defects, with a few occurrences in the millimeter size range, likely explaining their exceptionally poor performance in their group. Specimen 1B contained more sparse lack of fusion (five occurrences with sizes ranging between 124 μm and 248 μm), the longest life in the group and among all specimens measured via XCT. The fatigue performance of this specimen is relatively high despite the presence of LoF, presumably due to the sparsity and moderate size of these defects combined with the fine microstructure of set B. The XCT results are in agreement with the quantitative analysis of OT images (Fig. 4), according to which a higher number of spatter redeposits were detected in the gauge sections of the specimens located upstream in set B.

3.3.2. *Fractography*

Fig. 12 shows the fracture surfaces of specimens in set A. Most specimens had internal fracture crack initiation in features other than defects. Defects were identified in the crack initiation site of only two specimens, including the only specimen in this set where LoF were identified via XCT (12B). On the other hand, no defects were observed on the fracture surface of one of the poorest performing specimen in set A (11B; Fig. 13 d-f). Thus, a poorer performance is not necessarily associated to the presence of LoF. Surface initiation is more prevalent in specimens tested at the higher stress range.

The fracture surface of specimen 12B can be seen in detail in Fig. 13 (a–c), with a LoF of size of approximately 650 μm on the crack initiation site. Within the LoF, scan tracks and unfused powder particles are visible (Fig. 13c). Surrounding the defect, a faceted area (highlighted in with a white dotted line) is identified in both the SOM and SEM images. In the region where the fatigue crack propagated, radial marks pointing towards the defect are visible, and are indicated by white arrows. The region highlighted in blue sustained the final fracture.

In set B, most specimens contained LoF defects on the fracture surface (Fig. 14). In only four of the specimens (1A, 1B, 2B, 4B) no LoF were identified, all of which had above average lives in the group. The specimens in set B can be divided into two subgroups: one high-performing, with either no or few defects on the fracture surface, and one poor-performing, containing large defects on the fracture surface.

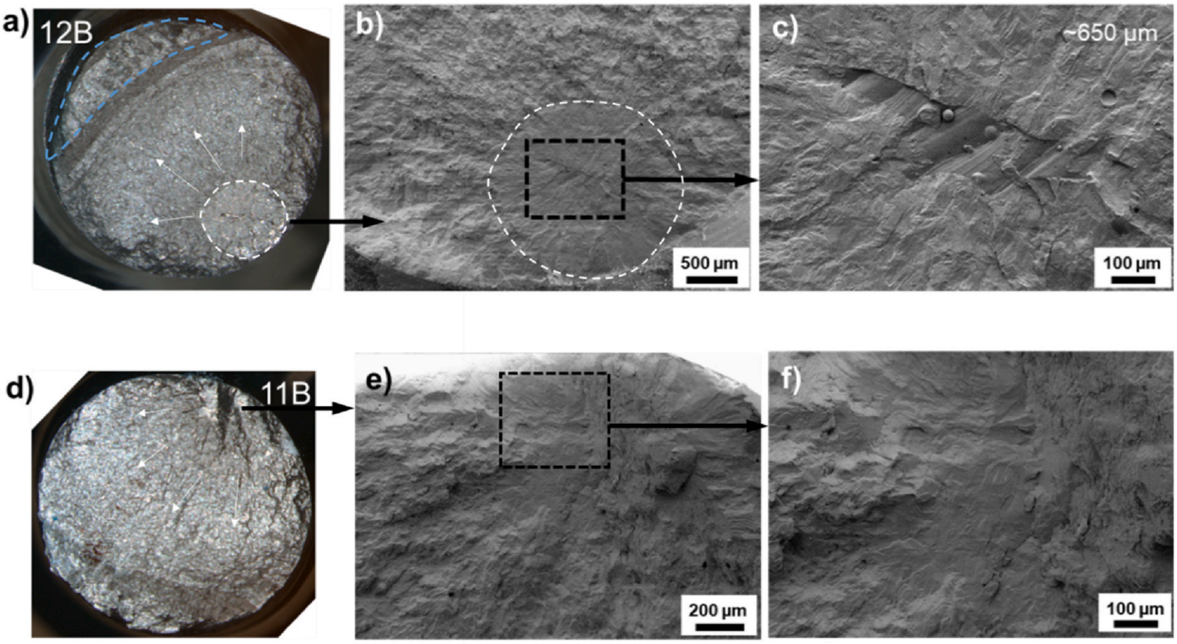

Fig. 13. Fracture surfaces of specimens 12B (a–c) and 11B (d–f), set A. The images were acquired with SOM (a, d) and SEM (b-c, e-f).

The specimens in the latter subgroup typically presented multiple, sizeable lack of fusion defects (see Fig. 15, Fig. 16), where scan tracks and powder particles are visible. In the former subgroup, fatigue cracks initiated either at the surface or in internal features other than defects, except for specimen 3B, where two lack of fusion defects were identified (Fig. 17). The smaller dimensions of these defects likely prevented the underperformance of this specimen within the group, despite their near-surface location and proximity to each other. The specimens belonging to the high-performing subgroup were all manufactured toward the gas outlet and had few spatter redeposit detections (Fig. 4).

As observed in the previous section, the limitation of oxygen content did not prevent the formation of LoF defects in either sets A and B. Moreover, these defects seem to have affected the fatigue performance of set B more significantly than the remaining sets. In the poor-performing subgroup of specimens in set B, the defect formation was too substantial to be counteracted by its finer microstructure in the same fashion as set 2 [26].

4. Discussion

This study aimed to assess whether restricting the oxygen content in the LPBF process atmosphere influences spatter-induced defect formation and consequently the mechanical performance of Hastelloy X, in particular fatigue.

4.1. Influence of oxygen content in spatter-induced defect formation

The presence of oxygen in contact with the melt pool has been attributed to augment spattering and its resulting defect formation [15,16] due to the modification in the melt pool dynamics [17,18]. While it has been demonstrated that the reduction of oxygen in process atmosphere reduces the surface oxidation of spatter particles [16,20], as well as the oxygen pickup in the bulk material [22], this study demonstrates that this modification in the process atmosphere does not reduce spatter-induced defect formation. Thus, the results indicate that other, non-oxygen-dependent factors, i.e., the disturbances introduced by the presence of spatter particles themselves [13,14], are the dominant factors determining the occurrence of spatter-induced defects in Hastelloy X.

4.2. Influence of spatter-induced defects on the fatigue performance of Hastelloy X

As established in the literature, defects are one of the main factors affecting fatigue performance of AM material [3,4]. In this study, it was shown that the defects formed by the less oxidized spatter particles are not less severe to fatigue performance, and that defect formation can even be more severe in cases where the oxygen content is reduced. Among the conditions analyzed in this study and in its precursor [26], set B manufactured with nominal layer thickness of 120 μm and 50 ppm O_2, contained the most numerous and largest lack of fusion defects, with multiple defects larger than 500 μm identified, including millimeter-sized defects. Comparatively, in set 2, manufactured in identical conditions except for the oxygen content set to maximum 1000 ppm, the largest defect measured was ~420 μm but multiple defects larger than 200 μm were observed.

The differences in fatigue performance of these two sets of Hastelloy X are evident (Fig. 10), presumably due to the differences in the defect populations. Nonetheless, in set 2, the finer microstructure obtained thanks to the larger nominal layer thickness was able to override the detrimental effects of defects in fatigue performance [26]. In the present study, this was not the case, despite the even finer microstructure of set B (Fig. 9b). In their study on fatigue performance of wire arc additive manufacturing of Ti–6Al–4V, Biswal et al. [38] proposed that the effect of defects dominates the fatigue performance, instead of the microstructure, if the defect size is larger than 8 times the microstructure characteristic length. Considering the average grain sizes (fitted ellipse major diameter) as the microstructure characteristic length, defects larger than ~400 μm and ~600 μm dominate fatigue performance in sets B and 2, respectively (Fig. 9b). In set 2, the largest measured defects were ~400 μm [26], which explains their limited influence on the fatigue performance. In the present study, while defect populations vary considerably among specimens based on their location on the build area during printing, defects larger than 400 μm are not uncommon in set B. In this set, many of the tested specimens had thus their fatigue performance steered by defects, resulting in short lives.

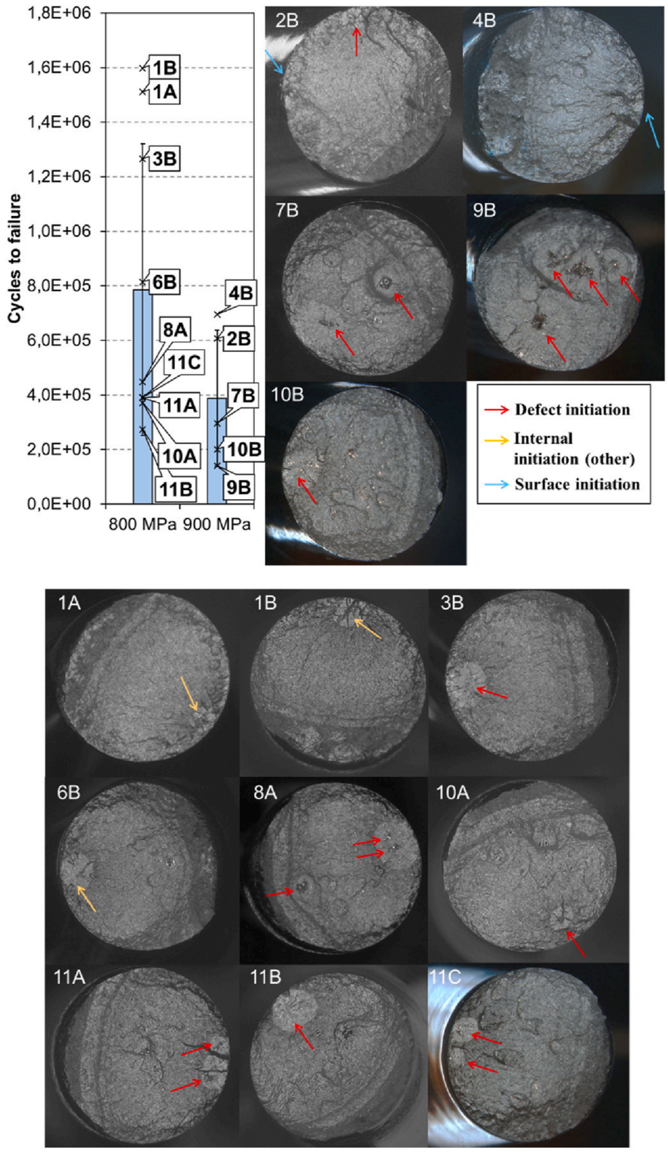

Fig. 14. Fracture surfaces of fatigue specimens in set B. The target stress ranges are indicated. The crack initiation sites are color-coded according to the type of initiation. The performance of each specimen is shown for reference.

The comparison between microstructure characteristic size and defect size explains why specimens demonstrably containing LoF could present good fatigue performance. Examples of that are specimen 3B in set B which contained two lack of fusion defects of sizes ~100 μm on the fracture surface (Fig. 17), and specimen 1B in set B, where five LoF (maximum size 248 μm) were found in XCT (Fig. 11c). Despite the proposal on critical defect size made by Biswal et al. [38] being based on an AM process other than LPBF, the principle seems to be transferable to LPBF and even other alloys, as Sanaei and Fatemi [4] also found that defects dominate the fatigue performance when their sizes are significantly larger than the microstructural characteristic length.

A conclusion common to the present study and its predecessor [26], apparently only abundant, large defects significantly affect the fatigue performance of LPBF Hastelloy X. A possible explanation for this observation is the high ductility of the material. The favorable effect of higher ductility on fatigue performance of specimens containing large defects has also been documented in other studies, e.g. Refs. [4,39], and is attributed to reduced notch sensitivity [4,40].

Note that this study aimed to investigate a potential mitigation strategy to spatter-induced defects, and their effect on mechanical properties, in particular fatigue, considering the premise that defects are the main factors driving performance on additively manufactured materials with post-processed surfaces [3]. With that, the microstructural analysis conducted is not exhaustive, as it was performed within the limited scope of supporting explanations to the mechanical properties measured beyond the presence of defects. Factors as major elemental segregation and strong texture [41], which have potential impact on the mechanical properties, were ruled out. More detailed and extensive microstructural and chemical analyses can be conducted in future work to provide further insights on the effect of changes in the process atmosphere on the microstructure.

4.3. *Distribution of spatter-induced defects on the build area*

As spatter particles are carried by the process gas towards the gas outlet, they are expected to accumulate in its adjacencies. Accordingly, detections of spatter redeposits are expected to occur predominantly in the areas of OT images depicting this region, as observed in previous work [6]. However, neither of the builds here analyzed presented such pattern (Fig. 4). Instead, most spatter redeposit detections were made in the central regions of the build area and toward the gas inlet. A possible reason for this behavior is distinct gas flow characteristics across builds, which influence the distribution of airborne particles on the build area.

Accordingly to the spatter redeposit detections spatial profile, part properties showed a strong dependency on their build location. Such issue has been previously found to be related to a lack of uniformity in the gas flow [42]. As for mitigation strategies, increasing the gas speed has been reported to improve the removal of process by-products from the build chamber [14], reduce the number of bulk defects [43,44] and improve mechanical performance [44]. However, an upper limit to the gas flow speed has also been reported [44], from which an increase in the gas flow promotes disturbances in the powder bed and leads to defect formation. Since an increased gas flow was needed to sustain a process atmosphere containing a maximum 50 ppm oxygen, this is likely the case in the experiments reported in the present paper. As pointed out by Weaver et al. [42], the degree and measure of uniformity necessary to avoid quality issues on LPBF is still to be determined. Detailed gas flow studies are necessary to elucidate the spatial distribution of spatter redeposits and resulting defects.

4.4. *Influence of a tighter control of the process atmosphere in the tensile properties of Hastelloy X*

Despite the finer microstructure of Hastelloy X produced with lower oxygen content (Fig. 9b), the measured yield and tensile strengths were not significantly different from the material produced with regular O_2 content and otherwise identical conditions (Fig. 5) [22].

Bulk chemical analysis showed that the material produced with a more controlled process atmosphere presented lower oxygen and nitrogen contents, which is explained by their lower partial pressure [22]. Further, EDS analysis showed that the oxygen is segregated, as expected and previously observed in LPBF Hastelloy X [32,36], on the cell boundaries. Thus, the decreased oxygen content in the process atmosphere is related to both finer microstructure, but also to a lower oxide formation on the cell boundaries, factors which have opposing effects on the impediment of dislocation motion, and therefore on the strengthening of the material. The combination of these factors explains the unaltered tensile and yield strengths observed among the different conditions analyzed.

The differences observed in ductility are possibly due to the differences in the defect contents of the sets of materials, as the presence of defects has been established to promote lower ductility [15,45,46]. It is important to note that defects do not usually compromise other tensile properties of additively manufactured materials, unless their dimensions and distribution significantly affect the effective load-bearing area [4].

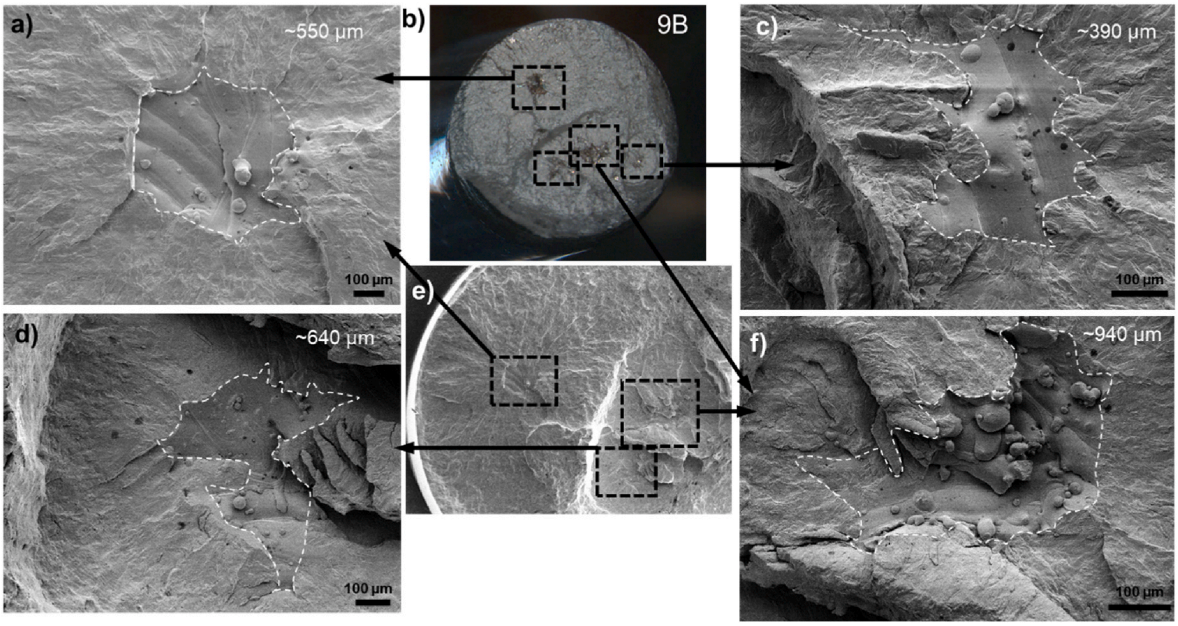

Fig. 15. Fracture surface of specimen 9B, set B. Multiple large crack-initiating defects were identified on the fracture surface; their sizes are indicated. The images were acquired with SOM (b) and SEM (a, c-f).

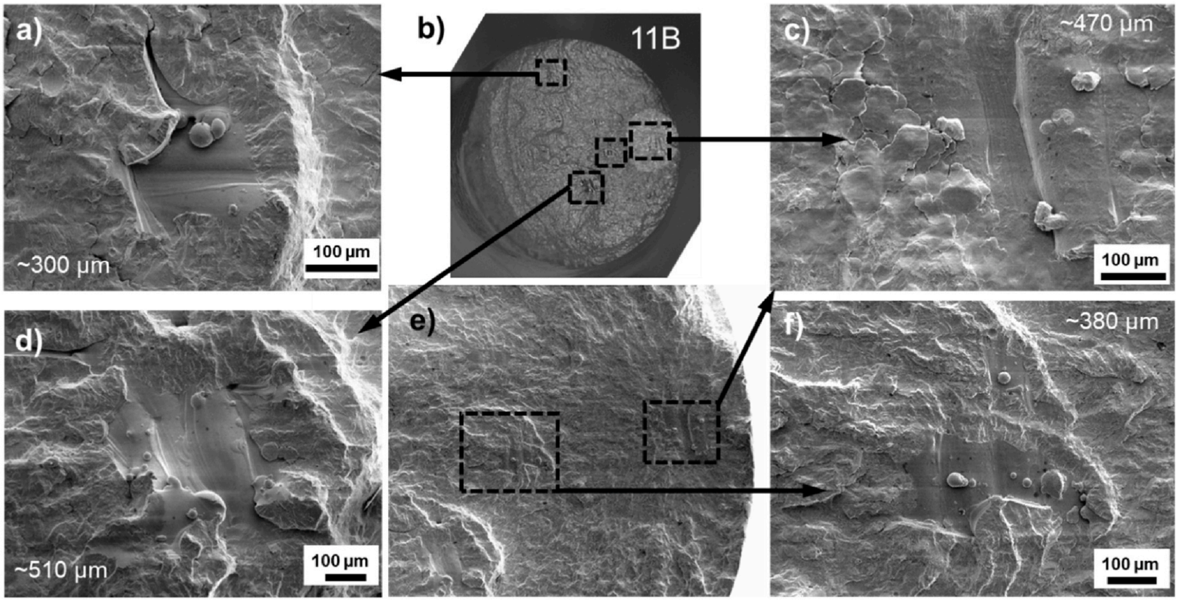

Fig. 16. Fracture surface of specimen 11B, set B. Multiple large lack of fusion defects were identified on the fracture surface; their sizes are indicated. The images were acquired with SOM (b) and SEM (a, c-f).

4.5. Further considerations

The current study suggests that the disturbance caused by the sole presence of spatter particles on the powder bed is the main contributing factor to defect formation. However, the collective processing conditions used in this study do not render the process particularly robust to the disturbances introduced by spatter particles [12]. While this was done by design in this study to provoke a significant amount of defects, the results might differ if conditions more robust to spatter-induced defects are studied instead (e.g. a smaller ratio between powder layer thickness and melt pool dimensions). Potentially, factors such as the specific surface oxide composition and morphology present on the particles may become predominant factors in determining the extent of defect formation [15–17]. These factors have already been found to differ for the specific varying condition examined in this study, with, e.g., a more severe selective oxidation of aluminum on the surface of spatter particles generated in process atmospheres with lower oxygen content [31].

5. Conclusions

In this study, the oxygen content in the LPBF process atmosphere was reduced from the usual 1000 ppm–50 ppm during the manufacturing of Hastelloy X with nominal layer thicknesses of 80 µm and 120 µm. The

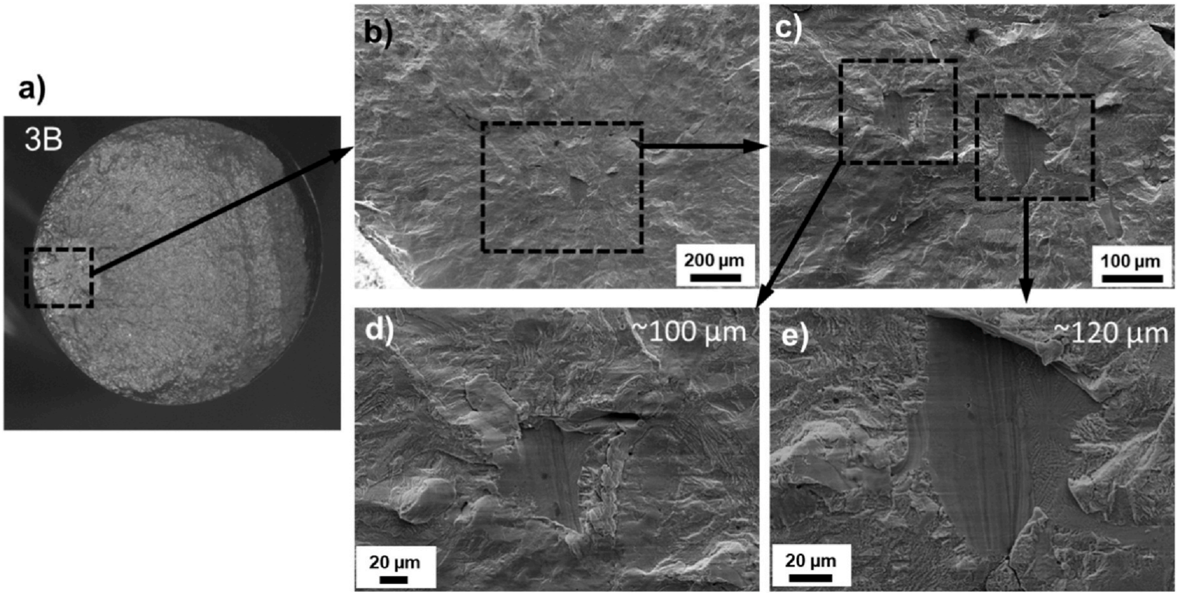

Fig. 17. Fracture surface of specimen 3B, set B. Two defects were identified on the initiation region of the fracture surface; their sizes are indicated. The images were acquired with SOM (a) and SEM (b–e).

effect of the reduction of the atmospheric oxygen content on spatter-induced defect formation and mechanical properties were evaluated.

Despite reducing the oxide thickness on the surface of spatter particles, the reduction of oxygen content in the process atmosphere does not prevent or reduce spatter-induced defect formation, suggesting that the disturbances promoted by spatter on the powder bed and its interaction with the laser beam are the dominant factors in this defect formation mechanism.

It was found that spatter-induced defect formation can even be more severe (more abundant and with larger defects) in cases where the oxygen content is reduced. On the other hand, the increase in gas flow needed for the tighter control of the process atmosphere promotes the formation of finer microstructure. If this finer microstructure is obtained in combination with scarce defects, an improvement in the fatigue performance is observed. The high ductility of Hastelloy X makes its fatigue performance rather insensitive to defects, occasionally even very large ones (~400 µm). However, if abundant defects much larger than the microstructural characteristic size are present, they dominate and degrade the fatigue performance.

The defect populations vary significantly among specimens in the same build job, which impacts the fatigue lives of individual specimens and promotes scatter in fatigue data. Qualitative analyses of OT images highlighting spatter trajectories and the extension of spatter formation do not necessarily correspond to the extent of spatters that redeposit within part boundaries and have the potential to form defects. Instead, the quantitative analysis of OT images, in which the spatter redeposits within part boundaries are computed, correlates with the defect populations found in the specimens measured by XCT and with the fatigue performance.

Declaration of competing interest

The authors declare that they have no known competing financial interests or personal relationships that could have appeared to influence the work reported in this paper.

Acknowledgements

This work was conducted within the framework of the projects DYNAMIQ (Quality assurance and dynamic response via on-line monitoring of additive manufacturing) funded by Vinnova (2022–02549), and MANUELA (Additive Manufacturing using Metal Pilot Line), funded by European Union's Horizon 2020 research and innovation programme under grant agreement no. 820774. This work was supported by the Competence Centre for Additive Manufacturing – Metal (CAM2), as well as the Production Area of Advance at Chalmers and LIGHTer Academy. The authors thank RISE Research Institutes of Sweden for lending the ADDvance O2 system, and Höganäs AB for the support with chemical analysis.

Appendix

Table 2
Tensile test results from sets A and B.

Specimen	Ultimate tensile strength (MPa)	Yield strength (MPa)	Elongation at fracture (%)
Set A, 1C	652	482	48
Set A, 7C	669	492	46
Set A, 12C	665	494	46
Set B, 1C	687	479	44
Set B, 7C	676	493	41
Set B, 12C	679	480	38

Table 3
Fatigue test results from sets A and B

Batch	Specimen ID	Number of cycles	Stress range (MPa)
Set A	1A	790 043	800
Set A	1B	724 069	802
Set A	2B	165 799	905
Set A	4B	1 141 880	802
Set A	5B	333 546	902
Set A	7B	1 411 926	801
Set A	8B	464 032	904
Set A	9B	1 170 196	806
Set A	10A	1 117 250	803
Set A	10B	272 985	908
Set A	11A	897 119	801
Set A	11B	692 311	801
Set A	12A	519 835	902
Set A	12B	788 642	804
Set B	1A	1 512 494	805
Set B	1B	1 599 521	803
Set B	2B	607 156	905
Set B	3B	1 266 538	802
Set B	4B	696 106	905
Set B	6B	814 525	803
Set B	7B	296 937	906
Set B	8A	448 488	805
Set B	9B	140 445	904
Set B	10A	371 874	800
Set B	10B	201 700	906
Set B	11A	390 034	797
Set B	11B	273 277	803
Set B	11C	391 570	801

References

[1] Sanaei N, Fatemi A. Progress in Materials Science Defects in additive manufactured metals and their effect on fatigue performance : a state-of-the-art review. Prog Mater Sci 2021;117(August 2020):100724. https://doi.org/10.1016/j.pmatsci.2020.100724.

[2] He X, et al. Powder recycling effects on porosity development and mechanical properties of Hastelloy X alloy during laser powder bed fusion process. Addit Manuf 2022;55(October 2021):102840. https://doi.org/10.1016/j.addma.2022.102840.

[3] Romano S, Brückner-Foit A, Brandão A, Gumpinger J, Ghidini T, Beretta S. Fatigue properties of AlSi10Mg obtained by additive manufacturing: defect-based modelling and prediction of fatigue strength. Eng Fract Mech Jan. 2018;187:165–89. https://doi.org/10.1016/J.ENGFRACMECH.2017.11.002.

[4] Sanaei N, Fatemi A. Analysis of the effect of internal defects on fatigue performance of additive manufactured metals. Mater Sci Eng, A 2020. https://doi.org/10.1016/j.msea.2020.139385.

[5] Snow Z, Nassar AR, Reutzel EW. Invited Review Article: review of the formation and impact of flaws in powder bed fusion additive manufacturing. Addit Manuf Dec. 01, 2020;36. https://doi.org/10.1016/j.addma.2020.101457. Elsevier B.V.

[6] Schwerz C, Raza A, Lei X, Nyborg L, Hryha E, Wirdelius H. In-situ detection of redeposited spatter and its influence on the formation of internal flaws in laser powder bed fusion. Addit Manuf Oct. 2021:102370. https://doi.org/10.1016/J.ADDMA.2021.102370.

[7] Li Z, et al. A review of spatter in laser powder bed fusion additive manufacturing: in situ detection, generation, effects, and countermeasures. Micromachines 2022;13(8). https://doi.org/10.3390/mi13081366.

[8] Mostafaei A, et al. Defects and anomalies in powder bed fusion metal additive manufacturing. Curr Opin Solid State Mater Sci 2022;26(2):100974. https://doi.org/10.1016/j.cossms.2021.100974.

[9] Simonelli M, et al. A study on the laser spatter and the oxidation reactions during selective laser melting of 316L stainless steel, Al-Si10-Mg, and Ti-6Al-4V. Metall. Mater. Trans. Phys. Metall. Mater. Sci. Sep. 2015;46(9):3842–51. https://doi.org/10.1007/s11661-015-2882-8.

[10] Raza A, et al. Degradation of AlSi10Mg powder during laser based powder bed fusion processing. Mater Des 2021;198(Jan). https://doi.org/10.1016/j.matdes.2020.109358.

[11] Fedina T, Sundqvist J, Kaplan AFH. Spattering and oxidation phenomena during recycling of low alloy steel powder in Laser Powder Bed Fusion. Mater Today Commun 2021;27(Jun). https://doi.org/10.1016/J.MTCOMM.2021.102241.

[12] Schwerz C, Bircher BA, Küng A, Nyborg L. In-situ detection of stochastic spatter-driven lack of fusion: application of optical tomography and validation via ex-situ X-ray computed tomography. Addit Manuf May 2023:103631. https://doi.org/10.1016/J.ADDMA.2023.103631.

[13] Esmaeilizadeh R, Ali U, Keshavarzkermani A, Mahmoodkhani Y, Marzbanrad E, Toyserkani E. On the effect of spatter particles distribution on the quality of Hastelloy X parts made by laser powder-bed fusion additive manufacturing. J Manuf Process Jan. 2019;37:11–20. https://doi.org/10.1016/j.jmapro.2018.11.012.

[14] Ladewig A, Schlick G, Fisser M, Schulze V, Glatzel U. Influence of the shielding gas flow on the removal of process by-products in the selective laser melting process. Addit Manuf 2016;10:1–9. https://doi.org/10.1016/j.addma.2016.01.004.

[15] Wang D, et al. Influence of spatter particles contamination on densification behavior and tensile properties of CoCrW manufactured by selective laser melting. Opt Laser Technol Jan. 2020;121:105678. https://doi.org/10.1016/j.optlastec.2019.105678.

[16] Tang M, Pistorius PC. Oxides, porosity and fatigue performance of AlSi10Mg parts produced by selective laser melting. Int J Fatig Jan. 2017;94:192–201. https://doi.org/10.1016/j.ijfatigue.2016.06.002.

[17] Leung CLA, Marussi S, Towrie M, Atwood RC, Withers PJ, Lee PD. The effect of powder oxidation on defect formation in laser additive manufacturing. Acta Mater Mar. 2019;166:294–305. https://doi.org/10.1016/j.actamat.2018.12.027.

[18] Delacroix T, Lomello F, Schuster F, Maskrot H, Garandet JP. Influence of powder recycling on 316L stainless steel feedstocks and printed parts in laser powder bed fusion. Addit Manuf Feb. 2022;50:102553. https://doi.org/10.1016/J.ADDMA.2021.102553.

[19] Köse C. Heat treatment and heat input effects on the dissimilar laser beam welded AISI 904L super austenitic stainless steel to AISI 317L austenitic stainless steel: surface, texture, microstructure and mechanical properties. Vacuum Nov. 2022;205:111440. https://doi.org/10.1016/j.vacuum.2022.111440.

[20] Raza A, Pauzon C, Hryha E, Markström A, Forêt P. Spatter oxidation during laser powder bed fusion of Alloy 718: dependence on oxygen content in the process atmosphere. Addit Manuf 2021;48(Dec). https://doi.org/10.1016/J.ADDMA.2021.102369.

[21] Schwerz C, Cao Y, Nyborg L. Surface chemical analysis of spatter particles generated in laser powder bed fusion of Hastelloy X in process atmospheres with high and low oxygen content. Surf Interface Anal Feb. 2023. https://doi.org/10.1002/SIA.7202.

[22] Dietrich K, Diller J, Dubiez-Le Goff S, Bauer D, Forêt P, Witt G. The influence of oxygen on the chemical composition and mechanical properties of Ti-6Al-4V during laser powder bed fusion (L-PBF). Addit Manuf 2020;32(July 2019). https://doi.org/10.1016/j.addma.2019.100980.

[23] Köse C. Fiber laser beam welding of additive manufactured 316L austenitic stainless steel with wrought 2507 super duplex and wrought 904L super austenitic stainless steels: crystallographic texture, microstructure, and mechanical properties. Vacuum Sep. 2023;215:112347. https://doi.org/10.1016/j.vacuum.2023.112347.

[24] Sims CT, Stoloff NS, Hagel WC. Superalloys II. second ed. Wiley; 1987.

[25] Xu J. High-performance nickel-based superalloys for additive manufacturing. 2022 [Online]. Available: https://urn.kb.se/resolve?urn=urn:nbn:se:liu:diva-184161. [Accessed 19 April 2024].

[26] Schwerz C, et al. Mechanical properties of Hastelloy X produced by laser powder bed fusion and affected by spatter redeposition. J Mater Res Technol Feb. 2024. https://doi.org/10.1016/J.JMRT.2024.02.150.

[27] Guo Q, et al. Transient dynamics of powder spattering in laser powder bed fusion additive manufacturing process revealed by in-situ high-speed high-energy x-ray imaging. Acta Mater Jun. 2018;151:169–80. https://doi.org/10.1016/j.actamat.2018.03.036.

[28] Schwerz C, Schulz F, Natesan E, Nyborg L. Increasing productivity of laser powder bed fusion manufactured Hastelloy X through modification of process parameters. J Manuf Process Jun. 2022;78:231–41. https://doi.org/10.1016/J.JMAPRO.2022.04.013.

[29] Bachmann F, Hielscher R, Schaeben H. Texture analysis with MTEX – free and open source software toolbox. Solid State Phenom 2010;160:63–8. https://doi.org/10.4028/WWW.SCIENTIFIC.NET/SSP.160.63.

[30] Pauzon C, et al. Impact of contour scanning and helium-rich process gas on performances of Alloy 718 lattices produced by laser powder bed fusion. Mater Des Mar. 2022:110501. https://doi.org/10.1016/J.MATDES.2022.110501.

[31] Raza A, Schwerz C, Pauzon C, Nyborg L, Hryha E. Effect of layer thickness on spatters oxidation of Hastelloy X alloy during powder bed fusion-laser beam processing. Powder Technol 2023;422(March):118461. https://doi.org/10.1016/j.powtec.2023.118461.

[32] Montero-Sistiaga ML, et al. Effect of temperature on the microstructure and tensile properties of micro-crack free hastelloy X produced by selective laser melting. Addit Manuf Jan. 2020;31:100995. https://doi.org/10.1016/J.ADDMA.2019.100995.

[33] Riabov D, Leicht A, Ahlström J, Hryha E. Investigation of the strengthening mechanism in 316L stainless steel produced with laser powder bed fusion. Mater Sci Eng, A Aug. 2021;822:141699. https://doi.org/10.1016/j.msea.2021.141699.

[34] Riabov D, Rashidi M, Hryha E, Bengtsson S. Effect of the powder feedstock on the oxide dispersion strengthening of 316L stainless steel produced by laser powder bed fusion. Mater Char Nov. 2020;169:110582. https://doi.org/10.1016/j.matchar.2020.110582.

[35] Kong D, et al. About metastable cellular structure in additively manufactured austenitic stainless steels. Addit Manuf Feb. 2021;38:101804. https://doi.org/10.1016/j.addma.2020.101804.

[36] He X, et al. Recrystallization effect on surface passivation of Hastelloy X alloy fabricated by laser powder bed fusion. J Mater Sci Technol Nov. 2023;163:245–58. https://doi.org/10.1016/j.jmst.2023.06.003.

[37] Snell R, et al. Methods for rapid pore classification in metal additive manufacturing. JOM Jan. 2020;72(1):101–9. https://doi.org/10.1007/s11837-019-03761-9.

[38] Biswal R, et al. Criticality of porosity defects on the fatigue performance of wire + arc additive manufactured titanium alloy. 2019. https://doi.org/10.1016/j.ijfatigue.2019.01.017.

[39] Cersullo N, Mardaras J, Emile P, Nickel K, Holzinger V, Hühne C. Effect of internal defects on the fatigue behavior of additive manufactured metal components: a comparison between Ti6Al4V and inconel 718. Materials 2022;15(19). https://doi.org/10.3390/ma15196882.

[40] Zhang M, et al. Fatigue and fracture behaviour of laser powder bed fusion stainless steel 316L: influence of processing parameters. Mater Sci Eng, A Aug. 2017;703:251–61. https://doi.org/10.1016/J.MSEA.2017.07.071.

[41] Sanchez-Mata O, Wang X, Muñiz-Lerma JA, Atabay SE, Attarian Shandiz M, Brochu M. Dependence of mechanical properties on crystallographic orientation in nickel-based superalloy Hastelloy X fabricated by laser powder bed fusion. J Alloys Compd Jun. 2021;865:158868. https://doi.org/10.1016/j.jallcom.2021.158868.

[42] Weaver JS, Schlenoff A, Deisenroth DC, Moylan SP. Inert gas flow speed Measurements in laser powder bed fusion additive manufacturing. National Institute of Standards and Technology Advanced Manufacturing Series; 2021. p. 100–43. https://doi.org/10.6028/NIST.AMS.100-43.

[43] Reijonen J, Revuelta A, Riipinen T, Ruusuvuori K, Puukko P. On the effect of shielding gas flow on porosity and melt pool geometry in laser powder bed fusion additive manufacturing. Addit Manuf Mar. 2020;32:101030. https://doi.org/10.1016/j.addma.2019.101030.

[44] Shen H, Rometsch P, Wu X, Huang A. Influence of gas flow speed on laser Plume attenuation and powder bed particle pickup in laser powder bed fusion. JOM Mar. 2020;72(3):1039–51. https://doi.org/10.1007/s11837-020-04020-y.

[45] Seifi M, Salem A, Satko D, Shaffer J, Lewandowski JJ. Defect distribution and microstructure heterogeneity effects on fracture resistance and fatigue behavior of EBM Ti–6Al–4V. Int J Fatig Jan. 2017;94:263–87. https://doi.org/10.1016/j.ijfatigue.2016.06.001.

[46] Soltani-Tehrani A, Isaac JP, Tippur HV, Silva DF, Shao S, Shamsaei N. Ti-6Al-4V powder reuse in laser powder bed fusion (L-PBF): the effect on porosity, microstructure, and mechanical behavior. Int J Fatig 2023;167(PB):107343. https://doi.org/10.1016/j.ijfatigue.2022.107343.